PSFC/JA-02-6

Observations and Empirical Scalings of the High-Confinement Mode Pedestal on Alcator C-Mod

J.W. Hughes, D.A. Mossessian, A.E. Hubbard,
B. LaBombard, E.S. Marmar

April 2002

Plasma Science and Fusion Center
Massachusetts Institute of Technology
Cambridge, Massachusetts 02139

Accepted for publication in *Physics of Plasmas*.

This work was supported in part by the U.S. Department of Energy Contract No. DE-FC02-99ER54512.

Observations and empirical scalings of the high-confinement mode pedestal on Alcator C-Mod

J.W. Hughes, D.A. Mossessian, A.E. Hubbard, B. LaBombard, E.S. Marmar

Abstract

On the Alcator C-Mod tokamak [Phys. Plasmas **1**, 1511, (1994)], radial profiles of electron temperature (T_e) and density (n_e) are measured at the plasma edge with millimeter resolution Thomson scattering [Rev. Sci. Instrum. **72**, 1107 (2001)]. Edge transport barriers in the high confinement regime (H-mode) exhibit T_e, n_e pedestals with typical widths of 2–6 mm, with the T_e pedestal on average slightly wider than and inside the n_e pedestal. Measurements at both the top and the base of the pedestal are consistent with profiles obtained using other diagnostics. The two primary H-mode regimes on C-Mod, enhanced D_α (EDA) and edge-localized mode free (ELM-free), have been examined for differences in pedestals. EDA operation is favored by high edge collisionality $\nu^\star$, in addition to high edge safety factor q_{95}. Scaling studies at fixed shape yield little systematic variation of pedestal widths with plasma parameters, though higher triangularity is seen to increase the n_e pedestal width dramatically. Pedestal heights and gradients show the clearest dependencies on plasma control parameters. Pedestal n_e and T_e both scale linearly with plasma current I_P, while pedestal T_e depends strongly on power flowing from the core plasma into the scrape-off layer $P_{\rm SOL}$. The electron pressure (p_e) pedestal and p_e gradient both scale with $I_P^2 P_{\rm SOL}^{1/2}$. Plasma stored energy W_P scales with pedestal p_e, implying that pedestal scalings may in large part determine global confinement scalings.

I. INTRODUCTION

In tokamaks, global transport and confinement depend strongly on temperature and density at the plasma edge,[1,2] which serve as boundary conditions for core plasma profiles. This dependence makes edge transport a topic of great interest in current and future fusion devices. Of particular interest is the edge transport barrier associated with the high confinement regime, or H-mode. The formation of this barrier produces a radially localized region of steep profile gradients. The result is a so-called pedestal, in both temperature and density, the parameters of which influence the core profiles and associated transport. This paper presents observations of the pedestal region on the Alcator C-Mod tokamak,[3] focusing on pedestal structure and scalings with plasma parameters.

C-Mod is a compact (major radius $R = 68$, minor radius $a = 22$ cm), high toroidal field ($B_T \leq 8$ T) tokamak that typically operates with plasma currents of 0.6–1.4 MA. H-mode discharges normally have a pedestal width of less than 1 cm. The phenomenology of the pedestal region is discussed in the following section, using measurements of electron density (n_e), temperature (T_e) and pressure (p_e) profiles from a millimeter resolution edge Thomson scattering (TS) system[4] and other edge diagnostics. Section III then describes the

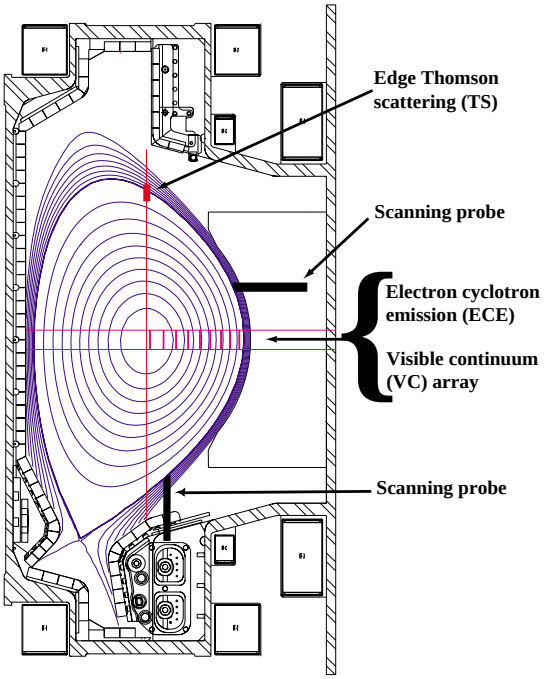

Figure 1: Schematic cross-section of Alcator C-Mod, showing surfaces of constant flux from a typical discharge and the poloidal locations of various edge diagnostic measurements.

two primary C-Mod H-mode operating regimes, edge-localized mode free (ELM-free) and enhanced D_α (EDA), and compares pedestals measured in ELM-free and EDA discharges. Particle transport differs considerably between these two regimes, and progress is made toward understanding the edge conditions that favor either regime. For EDA operation, several empirical scalings of T_e, n_e, and p_e pedestal parameters are presented in Sec. IV. The discharges examined herein all are in deuterium, having a single-null diverted geometry with ion ∇B drifts directed toward the X-point. Except for the ohmic H-mode mentioned in Sec. II, all discharges have auxiliary power supplied by ion cyclotron range of frequencies (ICRF) heating at 80 MHz, which is resonant with minority hydrogen ions at a field of 5.3 T.

II. PEDESTAL MEASUREMENTS

The C-Mod edge is diagnosed with a variety of instruments, including the TS system, a visible continuum (VC) array,[5] electron cyclotron emission (ECE) diagnostics and scanning Langmuir probes. These diagnostics measure T_e, n_e profiles at various poloidal locations, as shown in Fig. 1. Edge TS, ECE and probes measure local values, while the chord-integrated emissivities measured by the VC array are Abel inverted to unfold radial profiles. In order to compare profiles from the diagnostics, measurements are mapped along surfaces of constant flux to the midplane. The mapping is obtained from the results of the EFIT equilibrium reconstruction code,[6] which places the C-Mod separatrix with a radial uncertainty of approximately 3 mm. Because the pedestal is only a few millimeters in radial extent, relative offsets often must be applied to profiles, once they are mapped to the midplane, in order to

compare them properly. For the comparison to be meaningful, T_e and n_e must each be constant along a flux surface, a condition sometimes not met close to the X-point, particularly in high recycling regimes.[7] The measurements discussed herein are sufficiently removed from the X-point for the assumption of constant T_e, n_e along field lines to be reasonable.

A set of several parameters is used for describing and comparing the pedestals measured by various diagnostics. Each H-mode radial profile is described by its baseline (b), height (h), width (Δ), and location (R_0). These pedestal parameters are obtained by fitting profiles to a parameterized model function originally proposed by the DIII-D group.[8] The function is on midplane radius R:

$$f(R) = b + \frac{h}{2}\left[\tanh\left(\frac{R_0 - R}{d}\right) + 1\right] + m(R_0 - R - d)H(R_0 - R - d) \qquad (1)$$

Here $d = \Delta/2$ is the pedestal half-width. The Heaviside function, $H(R_0 - R - d)$, allows one to account for the finite radial slope, $-m$, that exists inside the pedestal region. At the base of the pedestal ($R = R_0 + d$), $f \approx b$; the value of f atop the pedestal ($R = R_0 - d$), is approximately $b + h$. Equation (1) has its maximum radial derivative at $R = R_0$: $|\nabla f|_0 = h/\Delta$. This notation will subsequently be used to denote the largest gradient of a given pedestal. Also, the subscript PED on a given variable will signify the value of that variable near the top of its pedestal (*e.g.*, $T_{e,\mathrm{PED}} = b_T + h_T$).

The edge TS system measures T_e and n_e with a nominal radial resolution of 1.3 mm after mapping along flux surfaces to the midplane. Typical profiles from edge TS extend from approximately 2 cm inside the LCFS to a point several millimeters outside the LCFS and in the near scrape-off layer (SOL). The dynamic range of the edge TS diagnostic is 15–800 eV, 3×10^{19}–5×10^{20} m^{-3}, which encompasses conditions throughout the pedestal region in most operational regimes. Figure 2 shows typical profiles of T_e, n_e and $p_e = n_eT_e$ measured in L and H-mode. The solid curves in the figure show the results of fitting the H-mode profiles to the tanh-like function of Eq. (1).

Most pedestal widths are in the range of 2–6 mm, with Δ_T slightly larger, on average, than Δ_n. This is shown in Fig. 3(a), which compares the distributions of n_e and T_e pedestal widths. The difference in the first moments of these distributions is approximately 0.5 mm. A similar scale length characterizes the average difference in radial position of the T_e and n_e pedestals. The distribution of $R_{0,T} - R_{0,n}$, shown in Fig. 3(b), is centered about -0.7 mm. The feet of the T_e and n_e pedestals, where the respective profile values tend toward b_T and b_n, both exist near the LCFS. The baseline values typically measure 15–30 eV and 3–5×10^{19} m^{-3}. Because the T_e profile is monotonic, and because SOL power balance requires $T_e > 30$ eV at the separatrix of almost all plasmas, we can conclude that the foot of the T_e pedestal lies slightly outside the LCFS. Pedestal gradients and quantities at the top of the pedestal in general depend on a number of plasma parameters, and the scalings with these parameters are discussed in Sec. IV.

Measurements of n_e and T_e in the SOL are made with two scanning probes, which are inserted into the SOL and withdrawn during a period of 50–100 ms, obtaining radial profiles with sub-millimeter resolution.[9] Figure 4 shows n_e and T_e profiles from a probe insertion into the pedestal of an ohmically heated H-mode, in which the penetration of the probe is sufficient to resolve most of the n_e pedestal profile. All but the innermost millimeter of the probe profiles agree favorably with the TS profiles, and no radial shifts of the data were

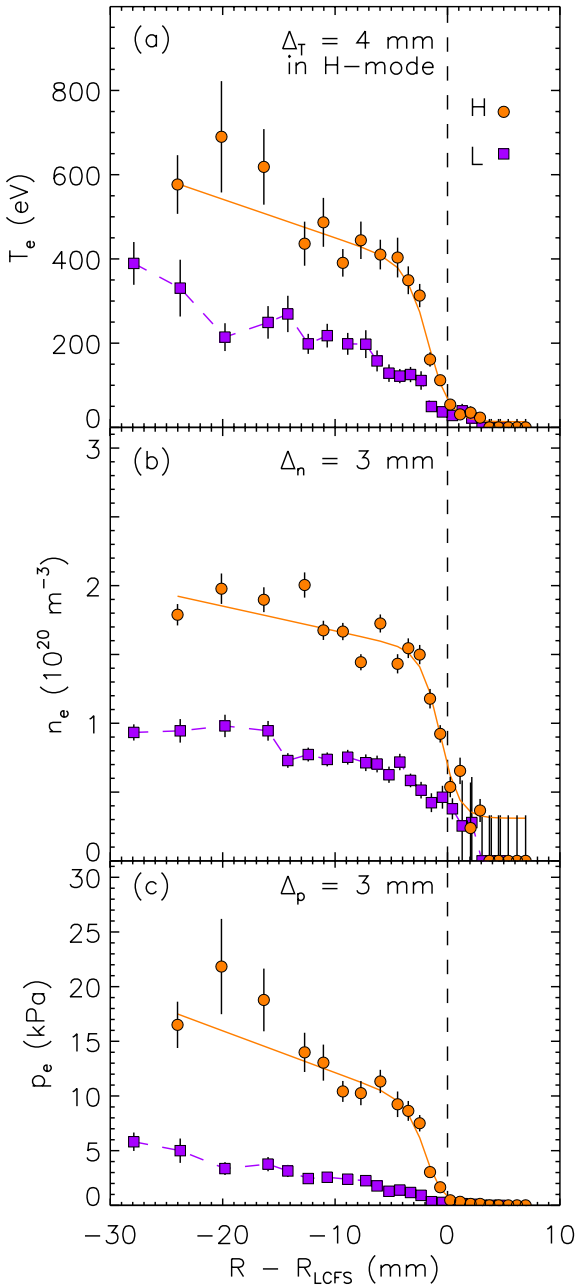

Figure 2: Profiles of electron temperature T_e (a), density n_e (b), and pressure p_e (c) from edge Thomson scattering (TS) immediately before (squares) and after (circles) an L-H transition. The solid curves represent the results of fitting the H-mode profile data to a tanh-like pedestal function. Also indicated are the numerical widths (Δ_T, Δ_n and Δ_p) from the pedestal fits. The vertical dashed line indicates the position of the last closed flux surface (LCFS).

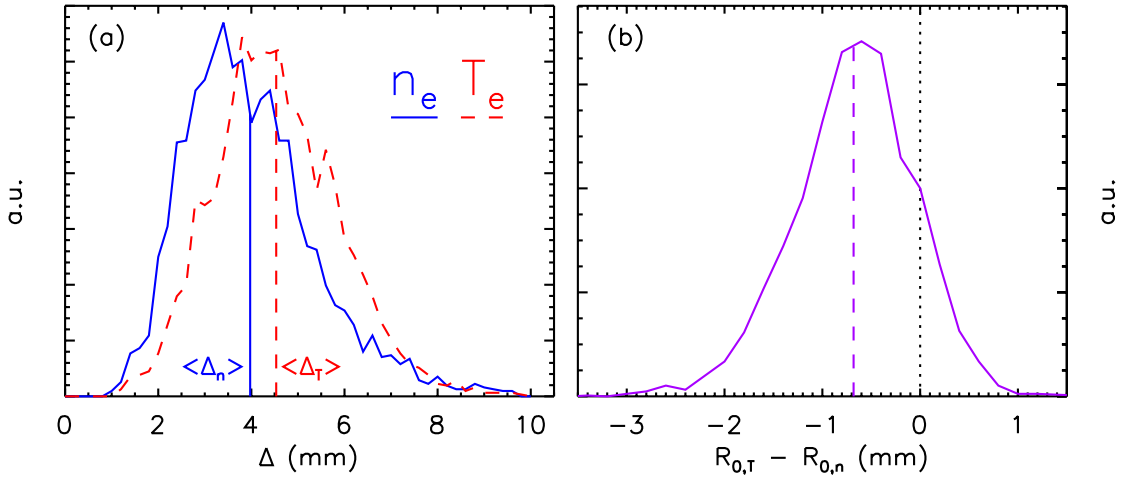

Figure 3: (a) Distributions of TS H-mode data points according to T_e, n_e pedestal widths. All types of H-mode are included. (b) Distribution of the difference in T_e, n_e pedestal radial position ($R_{0,T} - R_{0,n}$), of the same data.

required to obtain this agreement. Possible causes for the divergence of the profiles at high density and temperature include both overheating of the probe and actual perturbation of local conditions near the probe. In most H-mode plasmas, ICRF heating results in higher edge temperatures, which prevents insertion of the scanning probes into the pedestal region. However, the n_e and T_e profiles of the near SOL provide a useful extension of the edge TS data. The probes verify the TS measurement of pedestal baselines and also get data at densities below the sensitivity level of TS. Figure 4 shows that as the n_e and T_e profiles fall below the lower bounds of the edge TS dynamic range, denoted by the error bars on the zero measurements, probe data provides useful profile information.

We also match edge TS n_e with core profiles obtained from both core TS[10] and high-resolution VC measurements. The core TS measurements are made using the same laser source as those of edge TS, at six locations that are similarly mapped to midplane coordinates using EFIT equilibria. The midplane radii of the core measurements range from the magnetic axis to the plasma edge. The core TS system is optimized for higher T_e, n_e than the edge system, and has a spatial resolution on the order of 1 cm. There is consistent agreement between the diagnostics, within the experimental uncertainties of each. The VC measurements are made at the midplane with a tangentially-viewing CCD array, filtered for wavelengths in a narrow band about $\lambda_0 = 536$ nm. The chord integrated measurement undergoes an Abel inversion to produce millimeter resolution radial profiles of plasma emissivity. We use the assumption that, above 20 eV, the continuum at this wavelength is dominated by free-free bremsstrahlung, and, by the technique described in Refs. 5 and 11, we obtain a high resolution core n_e profile throughout the plasma.

ECE diagnostics give additional measurements of T_e. Two grating polychromators are used, giving measurements of T_e at up to 28 values of midplane radius. To obtain highly resolved T_e profiles with ECE, we insert a 2–3% modulation in the toroidal field B_T, which sweeps radially the ECE measurement positions and yields a T_e profile with 9 mm instrument

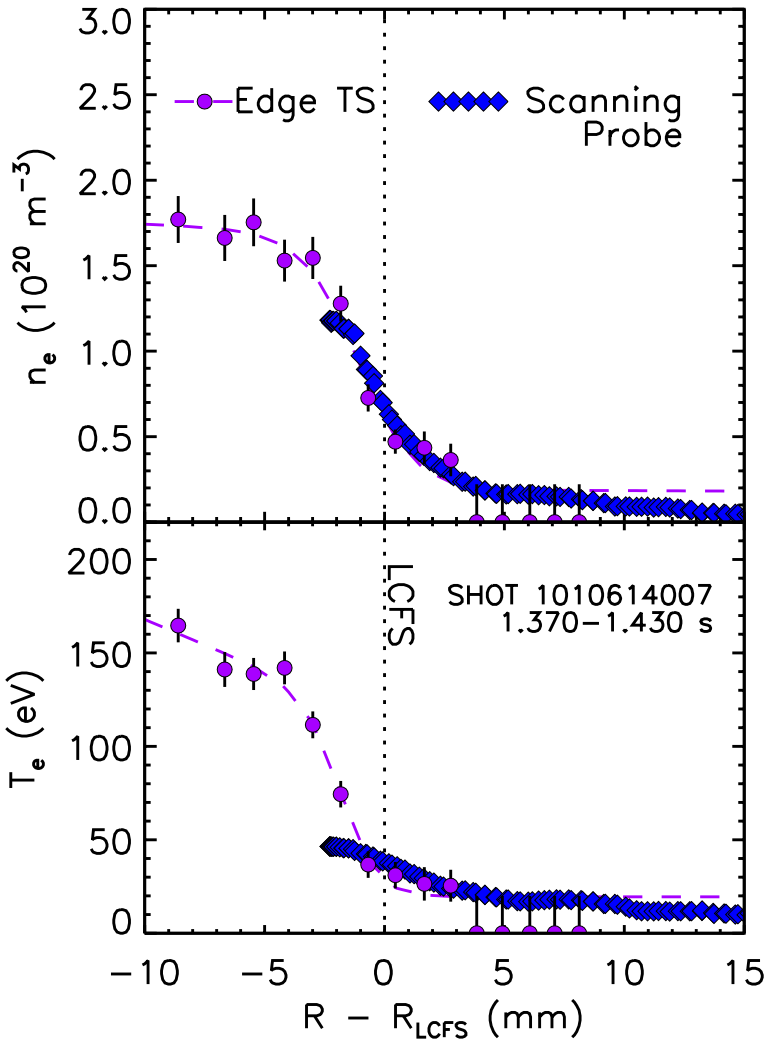

Figure 4: Comparison of edge TS profiles (circles) of n_e, T_e with a 60 ms scanning probe plunge (diamonds) through the last closed flux surface (LCFS) of an ohmic H-mode discharge (toroidal field $B_T = 3.4$ T, plasma current $I_P = 0.73$ MA). TS data are average values from profiles measured during the probe scan; dashed curves represent tanh fits to the TS profiles.

limited resolution.[12] The typical time scale for such a sweep is 100 ms.

The plots in Fig. 5 show profiles produced by the simultaneous use of the above techniques. In this example, a steady H-mode discharge was maintained, and B_T was swept from 5.4 to 5.6 T and back over a period of 200 ms. Within this time the scanning probes were driven through the SOL into the vicinity of the LCFS. Six TS time points are averaged to reduce the level of statistical uncertainty in the TS profiles. VC data are also time-averaged. Relative radial shifts of -0.5 and 1.0 mm, respectively, are applied to the probe and VC profiles to bring them into alignment with the TS profiles. Uncertainties in position calibrations and flux surface mapping easily can account for these offsets. The ECE radii, which are determined from the measured magnetic field, are shifted 9.5 mm relative to the TS midplane radii. An error of approximately 1% in the calibration of the B_T measurement would justify a centimeter radial shift, though the calculated uncertainty of this calibration is within 0.5%.[13] We find that the offset is systematic, and as a result all ECE profiles shown in this paper have required translation by approximately 1 cm.

The profiles in Fig. 5 illustrate typically good agreement, after correction for errors in radial coordinates, among the C-Mod diagnostics observing the plasma edge, within the experimental uncertainties of each. Profiles from TS agree with probe data in the SOL, while the core profiles match ECE and VC measurements very well. The discrepancy between the ECE and TS profiles in the pedestal region is explained by the larger spatial resolution of the ECE diagnostic. Several millimeters inside the LCFS, gradients relax, and ECE and edge TS produce mutually consistent profiles of core plasma T_e. There is also good overall agreement between TS and VC. Though the profiles in Fig. 5(a) seem to show small variations in n_e atop the pedestal, these are actually related to measurement uncertainties. In the case of TS, there are uncertainties of 5–10% in absolute calibration coefficients, which vary channel to channel. The local maximum present in the VC inversion is not a real pedestal structure, since it appears even during the L-mode portion of this discharge. It may be the result of an unwanted reflection within the machine.

Both profiles exhibit core gradients roughly constant in R, with gradient scale lengths such that $L_T < L_n$ ($L_T = |T_e/\nabla T_e|$, $L_n = |n_e/\nabla n_e|$). An interesting feature in the T_e profile, observed in a number of steady H-mode discharges, is a region of T_e gradient intermediate between that in the pedestal ($|\nabla T_e| \sim$ 50–100 keV/m, typically) and that in the core plasma ($|\nabla T_e| \sim$ 5–10 keV/m). This region is located immediately inside the T_e pedestal and is approximately 1 cm in radial extent. The change in T_e gradient in this region has been observed with both ECE and edge TS, though the adjacent pedestal seen with edge TS is too localized to be measured with ECE. Thus, fitting Eq. (1) to ECE profiles generally results in pedestals that are wider (> 1 cm) and hotter than those from edge TS. We can infer that similar instrumental differences could also impact the comparison of pedestal data of different machines, and that the simple tanh-like equation may insufficiently model H-mode edge temperature and pressure profiles on C-Mod. The remainder of this paper will focus on T_e and n_e measurements from TS, and only the edge TS profiles, mapped to the midplane, are fit to the tanh-like function. Absolute radial position of the pedestals is not considered, and therefore radial uncertainties in the EFIT placement of the separatrix should have no effect on the chief results of Secs. III and IV.

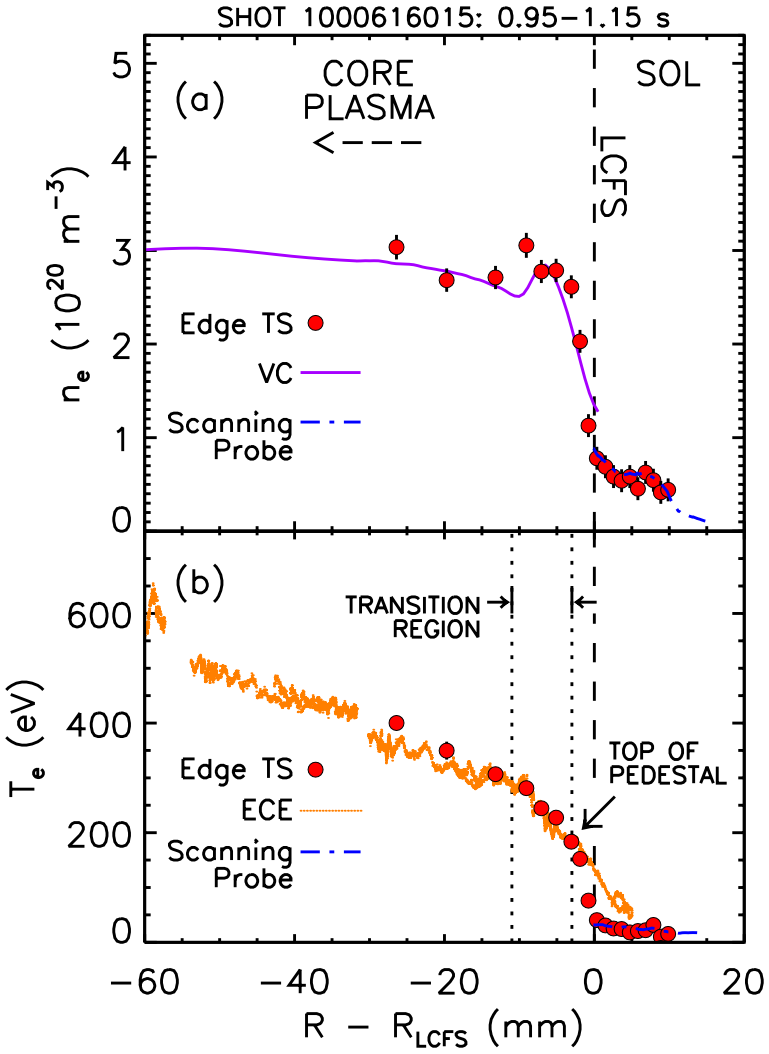

Figure 5: Combined profiles of (a) n_e and (b) T_e near the C-Mod edge from multiple diagnostics during a toroidal field sweep between 5.4 and 5.6 T. Scanning probes are used in the scrape-off layer (SOL), while core profiles are obtained with visible continuum (VC) and electron cyclotron emission (ECE) measurements. Edge TS resolves the region about the LCFS. VC and edge TS data are time-averaged over 200 ms. The T_e profile shows a transition region approximately 1 cm in width between the pedestal and core, exhibiting $|\nabla T_e|$ intermediate between pedestal and core gradients.

III. PEDESTAL CHARACTERISTICS IN EDA AND ELM-FREE H-MODES

On C-Mod two major categories of H-mode are observed. The ELM-free regime has low levels of edge particle transport and no edge-localized modes (ELMs),[14] and is characterized by increasing core density and impurity concentration, leading to termination of the H-mode by radiative collapse. More common is the enhanced D_α (EDA) H-mode,[15–17] so named because measured D_α intensity is much larger than that in ELM-free operation. Energy confinement in EDA H-mode is near that of ELM-free, but particle confinement is reduced, allowing a steady H-mode to be maintained with constant density and stored energy, and with no accumulation of impurities. EDA H-modes can be maintained for many energy confinement times with the application of steady ICRF heating and without the presence of large Type I ELMs. It has been shown experimentally[16–18] that the enhanced particle transport of EDA is driven by a quasi-coherent (QC) fluctuation ($f \sim 100$ kHz, $k_\theta \sim 1$–5 cm^{-1}) localized to the pedestal region. Because of the absence of large ELMs and the steady-state aspect of EDA, it has drawn interest as a possible reactor regime and has been examined extensively. Of particular interest are the conditions favoring EDA and how these conditions give rise to the QC mode. Experiments show[16] that EDA is favored by both high edge safety factor ($q_{95} \gtrsim 3.7$) and high triangularity ($\delta \gtrsim 0.3$). Discharges at fixed shape and magnetic configuration show a threshold also in target density, the average density prior to L-H transition, below which H-modes are ELM-free and do not exhibit the QC mode.[17,19]

The localization of the QC mode to the pedestal region leads us to examine the operational space for EDA in terms of pedestal parameters. Edge TS data are categorized according to either the presence or the absence of the QC mode, as observed using either reflectometry[20] or phase contrast imaging[21] diagnostics. Measurements of n_e and T_e at mid-pedestal are plotted in Fig. 6 for both low and high values of edge q. Because pedestal safety factor is not well known, values of q at the 95% flux surface from EFIT equilibria (ranging from 3.2 to 6.5) are used to group the data. Because C-Mod typically runs at $B_T \approx 5.4$ T and often at one of three discrete values of current ($I_P = 0.8, 1.0, 1.2$ MA), the data naturally fall into three clusters corresponding to $q_{95} \approx 3.4, 4.0, 4.8$. Here we choose $q_{95} = 3.7$ as a convenient boundary between low q operation (the first cluster of data) and high q operation (the second and third clusters). For low q [Fig. 6(a)], H-modes are predominately ELM-free. However, the QC mode can exist even at these q, provided mid-pedestal n_e is above 1.3–1.5$\times 10^{20}$ m^{-3}. We find no such density threshold for high q operation [Fig. 6(b)], where EDA predominates. For mid-pedestal $T_e \gtrsim 200$ eV, the QC mode disappears, leading to ELM-free operation. It is unclear from Fig. 6(a) whether a similar T_e threshold exists at low q, high n_e (above dotted line). Taken altogether, the tendency for EDA operation at higher q_{95} and pedestal n_e and lower pedestal T_e suggests that edge collisionality $\nu^\star$ plays an important role in determining the existence the QC mode. Collisionality is defined as the ratio of the effective electron-ion collison frequency to the bounce frequency,

$$\nu^\star = \frac{\nu_{\text{eff}}}{\nu_b} = \frac{qR\nu_{ei}}{\epsilon^{3/2} v_{\text{th},e}} \tag{2}$$

where ϵ is inverse aspect ratio and $v_{\text{th},e}$ is the electron thermal speed. At fixed shape, $\nu^\star \propto q n_e \ln\Lambda / T_e^2$, where the Coulomb logarithm varies weakly with n_e, T_e ($\ln\Lambda \approx 15$). A contour of constant $\nu^\star$ at fixed q is represented by the dashed curve in Fig. 6(b), perhaps denoting a boundary between EDA and ELM-free operation. Here EDA operation occurs

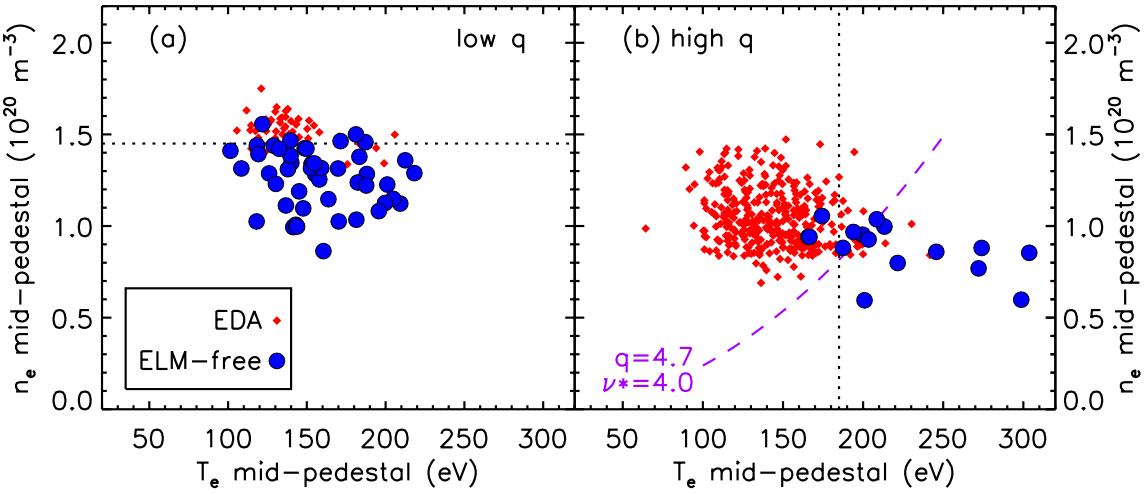

Figure 6: Operational space of EDA (diamonds) and ELM-free H-modes (circles). T_e, n_e are taken at the point of maximum pedestal gradient. Data are from (a) low q ($3.2 < q_{95} < 3.7$) and (b) high q ($3.7 < q_{95} < 6.5$) discharges with average triangularity $\delta_{\rm AV}$ between 0.35 and 0.45. Dotted lines represent apparent thresholds for EDA in parameter space. The dashed curve in (b) represents a contour of constant collisionality $\nu^\star$ at fixed q.

mainly at $\nu^\star \gtrsim 4$. In contrast the EDA points at low q exist at considerably higher values of $\nu^\star$, and it is not possible to construct a parabolic curve of constant collisionality that satisfactorily separates the EDA and ELM-free points in Fig. 6(a). A collisionality threshold alone is therefore insufficient to explain the appearance and disappearance of the QC mode, at least at low q.

The low q data can be plotted in terms of $\nu^\star$ and pedestal electron pressure gradient $|\nabla p_e|_0$, as in Fig. 7. The indication from this figure is that at low q and low collisionality, EDA operation is possible at higher values of pressure gradient. When we examine high q discharges, however, the pressure gradients in EDA and ELM-free discharges are very similar, and too few ELM-free data exist to conclude what effect, if any, pressure gradient has on determining the presence of the QC mode. Nonetheless, a very clear boundary between EDA and ELM-free operation can be observed in terms of $\nu^\star$ and normalized pressure gradient,[22]

$$\alpha = -\frac{2\mu_0 q^2 R}{B^2}\frac{dp}{dr} \tag{3}$$

a dimensionless parameter developed from the theory of ideal magnetohydrodynamics for the assessment of stability to high n ballooning modes. Figure 8 represents all data from Fig. 6 in α-$\nu^\star$ space, where we have evaluated $\nu^\star$ and q at the 95% flux surface, and the maximum pedestal p_e gradient is taken for dp/dr. Rendering the data in this way allows us to recast in one phase space the separations beteen EDA and ELM-free operation evident in both Figs. 6(b) and 7. The α parameter depends on both q and ∇p. Considerable overlap of EDA and ELM-free data occurs for low q discharges if we fail to account for pressure gradient and simply plot $\nu^\star$ *vs.* q^2 or $\nu^\star$ *vs.* q. Also, there is virtually no operational boundary to be observed if we neglect q and examine only $\nu^\star$ *vs.* ∇p_e.

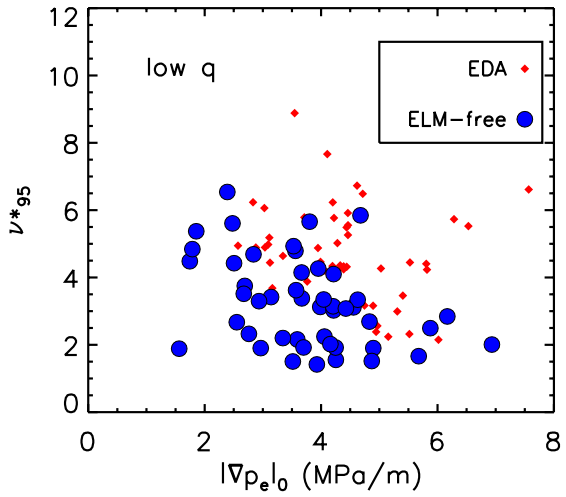

Figure 7: EDA (diamonds) and ELM-free H-modes (circles) at low q_{95}. Here collisionality at the 95% flux surface ν^*_{95} is plotted against maximum electron pressure gradient $|\nabla p_e|_0$. Even at low collisionality, EDA can be obtained with sufficient pressure gradient.

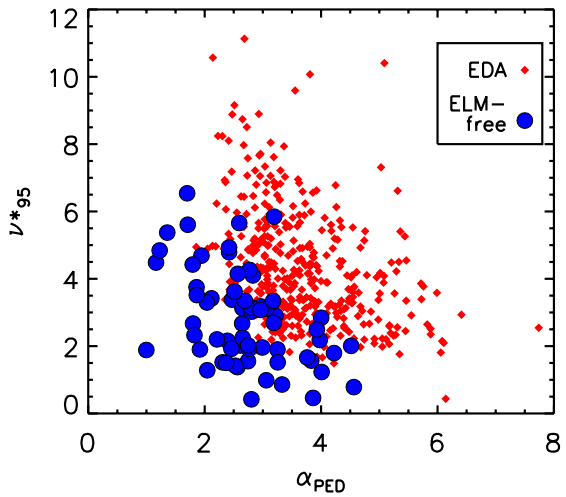

Figure 8: Operational space of EDA (diamonds) and ELM-free H-modes (circles). Here $\alpha_{\rm PED}$ is proportional to $(q^2_{95}R)/B^2_T \times |\nabla p_e|_0$. Larger values of each quantity favor EDA operation.

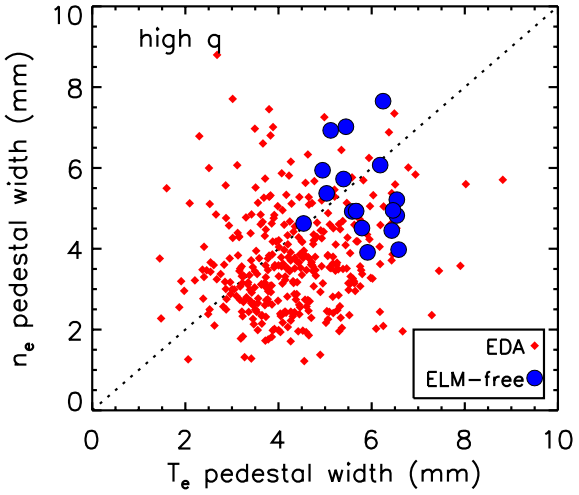

Figure 9: Operational Δ_T-Δ_n space of EDA (diamonds) and ELM-free H-modes (circles) in high q discharges with $0.35 < \delta < 0.45$.

There is no clear contrast in pedestal widths between EDA and ELM-free H-modes at low values of q_{95}. However, for high q, Fig. 9 shows that widths of T_e, n_e pedestals are larger on average in ELM-free (4–7 mm) than in EDA (2–6 mm). Though the maximum T_e gradient is smaller on average in high q EDA operation than in high q ELM-free operation (due to the requirement that pedestal T_e should not be too large), the n_e gradients are systematically larger than in ELM-free. This increased $|\nabla n_e|$ occurs despite the enhanced particle transport of EDA. As mentioned above, the p_e gradient at high q shows little variation between EDA and ELM-free discharges.

IV. SCALING STUDIES

Global confinement on C-Mod is correlated strongly with edge conditions, since both core thermal gradients and energy confinement time increase as edge temperature is raised.[1] Similar results are reported on other experiments as well.[2] Because confinement and edge conditions are tightly coupled, extrapolation of pedestal parameters to reactor-scale devices is of great interest. The factors determining pedestal widths and heights in tokamaks are not yet well understood, despite experimental efforts on major experiments, including JT-60U, DIII-D, ASDEX Upgrade, JET, and C-Mod. This experimental work, along with theoretical predictions of pedestal scalings are reviewed in some detail in Ref. 23. Here we present the results of recent studies intended to determine empirical T_e, n_e and p_e pedestal scalings on C-Mod.

A large amount of scatter exists in the pedestal parameters derived from edge TS profiles, which complicates the interpretation of pedestal scalings. There appear to be comparable contributions to the variance in the data from both statistical uncertainty and actual edge fluctuations. To reduce scatter, TS and other plasma measurements are time averaged over periods of finite and constant input ICRF power, $P_{\rm RF}$, with stored energy, W_P, changing by less than 10%. Restricting study to steady discharges requires that only EDA H-modes be in-

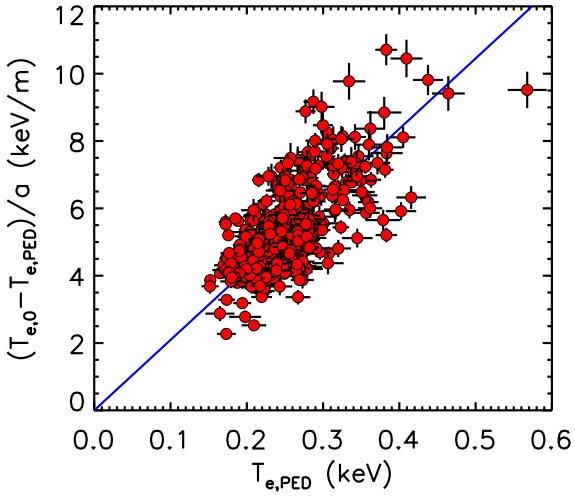

Figure 10: Characteristic core T_e gradient *vs.* pedestal T_e in EDA H-modes on C-Mod. Measurements are from the central core TS channel ($T_{e,0}$) and the edge TS pedestal fit ($T_{e,\mathrm{PED}}$).

cluded in the remaining analysis. Discharges that exhibit small ELMs or impurity injections are also excluded from study, since the associated pedestals have significant transient variations. To broaden the range in dependent parameters, we conducted dedicated experiments in which steady discharges were run at various plasma currents ($0.6 < I_P[\mathrm{MA}] < 1.2$), magnetic fields ($4.5 < B_T[\mathrm{T}] < 6.0$), and target densities ($1.3 \times 10^{20} < \bar{n}_{e,L}[\mathrm{m}^{-3}] < 2.6 \times 10^{20}$). Here $\bar{n}_{e,L}$ is defined as the line averaged density immediately prior to transition from L to H-mode. H-modes were triggered and maintained with steady P_{RF}, which was varied between discharges in the range of 1–3 MW. RF absorption is on minority H ions, and heating efficiency η_{RF} is known to drop if the minority fraction in the plasma becomes too high. For this reason, when an accurate global power balance is needed for scaling studies, discharges with $n_{\mathrm{H}}/(n_{\mathrm{H}} + n_{\mathrm{D}}) > 0.08$ are excluded. Plasma shaping, as discussed later in this section, can strongly affect the pedestal. For these studies only a standard C-Mod equilibrium is considered, having $R = 68$ cm, $a = 22$ cm, elongation $\kappa = 1.7$, and average triangularity $\delta_{\mathrm{AV}} = 0.4$.

TS data support the notion that the edge pedestal acts as a boundary condition to set core transport and confinement. Figure 10 shows the characteristic core electron temperature gradient, given by $(T_{e,0} - T_{e,\mathrm{PED}})/a$, as a function of pedestal T_e. Here $T_{e,0}$ is measured by the central core TS channel, and $T_{e,\mathrm{PED}}$ is from edge TS. The linear dependence of the core thermal gradient on edge T_e corroborates previous results on C-Mod[1] and suggests the core profile may be determined by a critical gradient scale length for ion temperature,[24] which for characteristic C-Mod densities should be tightly coupled to the measured T_e. Also, total plasma stored energy has a nearly linear correlation with pedestal pressure, as shown in Fig. 11. An implication of this result is that scaling laws for energy confinement time τ_E should be closely linked to scalings of the pressure pedestal with parameters that we control, such as plasma current, magnetic field, and input power.

Of particular interest is the manner in which pedestal widths Δ scale with plasma pa-

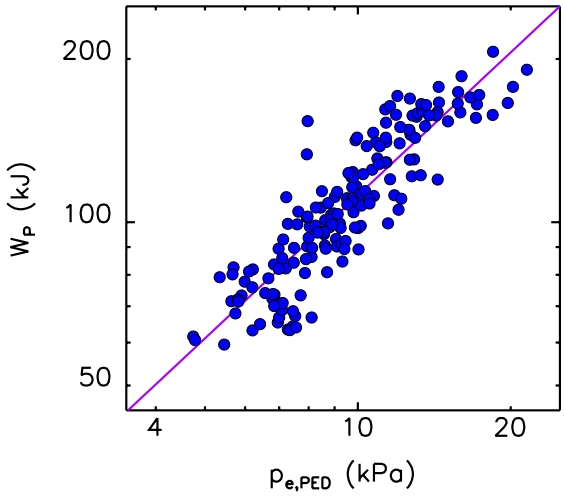

Figure 11: Relation of global plasma energy W_P to the electron pressure pedestal $p_{e,\mathrm{PED}}$ in EDA H-modes. The best power law fit to the data gives $W_P \propto (p_{e,\mathrm{PED}})^{0.88\pm0.03}$.

rameters, since, for a given pedestal gradient, Δ determines the pedestal height. On C-Mod, at a fixed shape, there is no clear systematic variation in the electron temperature and pressure pedestal widths Δ_T and Δ_p. This contrasts with results reported on DIII-D[25] and JT-60U[26] that demonstrate width variation with I_P and edge T_e. Theoretical predictions[23] that pedestal width should scale with poloidal ion gyroradius $\rho_{i,\mathrm{POL}}$ do not appear to hold on C-Mod, though the measured Δ are of the same order as $\rho_{i,\mathrm{POL}}$. The lack of correlation is illustrated specifically for Δ_p in Fig. 12. The invariance of T_e and p_e pedestal width is similar to results on ASDEX-Upgrade,[27] in which Δ_p is invariant as I_P is scanned and global

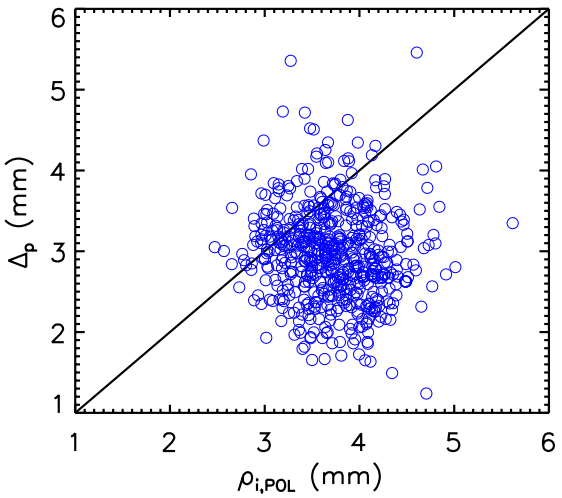

Figure 12: C-Mod pressure pedestal width Δ_p *vs.* poloidal ion gyroradius $\rho_{i,\mathrm{POL}}$, in a variety of EDA H-modes. No correlation is observed.

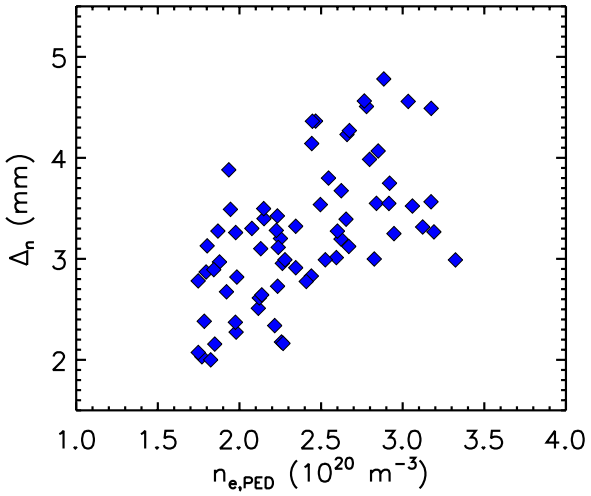

Figure 13: Density pedestal width *vs.* n_e atop pedestal in EDA H-modes at 5.4 T and fixed L-mode target density, $\bar{n}_{e,L} \sim 1.6 \times 10^{20}$ m^{-3}. Higher density favors larger Δ_n.

confinement correlates equally well with either $p_{e,\mathrm{PED}}$ or pedestal ∇p_e. Interestingly, higher pedestal n_e favors larger Δ_n on C-Mod, as shown in Fig. 13, a result that contrasts with recent DIII-D results[28] that show Δ_n scaling with $1/n_{e,\mathrm{PED}}$. The indication is that, unlike ∇T_e and ∇p_e, density pedestal gradient varies weakly on C-Mod.

In contrast to the widths, pedestal heights and gradients show clear scalings with control parameters. Electron temperature profiles from edge TS and ECE, obtained in identical discharges with varied levels of ICRF power, are shown in Fig. 14. As P_{RF} is raised, the T_e pedestal rises, both in height and gradient, while the width remains constant. The n_e pedestals are unchanged in these three discharges. We find that, when other control parameters are held constant, both pedestal T_e and $|\nabla T_e|_0$ can be scaled in terms of the power passing into the scrape-off layer P_{SOL} given by the power balance relation,

$$P_{\mathrm{SOL}} = P_{\mathrm{OH}} + \eta_{\mathrm{RF}} P_{\mathrm{RF}} - P_{\mathrm{RAD}} - \frac{dW_P}{dt} \tag{4}$$

where both the rate of change in plasma stored energy dW_P/dt and the core radiated power measured from bolometry P_{RAD} are subtracted from the ohmic power P_{OH} and auxiliary heating power $\eta_{\mathrm{RF}} P_{\mathrm{RF}}$. For each discharge analyzed we calculate P_{SOL}, assuming an ICRF heating efficiency $\eta_{\mathrm{RF}} = 0.8$. Figure 15 plots the T_e pedestal and its gradient as a function of P_{SOL} for discharges made during pedestal scaling experiments, all having the same B_T and the same target density $\bar{n}_{e,L}$. It is evident that $T_{e,\mathrm{PED}}$ and $|\nabla T_e|_0$ scale with power in a similar fashion. In the transition region between pedestal and core, T_e closely tracks $T_{e,\mathrm{PED}}$ such that, on average, $T_{e,95} \approx 1.05 \times T_{e,\mathrm{PED}}$. Analysis that uses $T_{e,95}$ as an estimate of H-mode pedestal height should be valid in general, and, in fact, the characteristic temperature of the transition region, which may be approximated by $T_{e,95}$, could be the crucial boundary condition that influences core confinement. For the remainder of this paper, however, only the T_e pedestal will be considered.

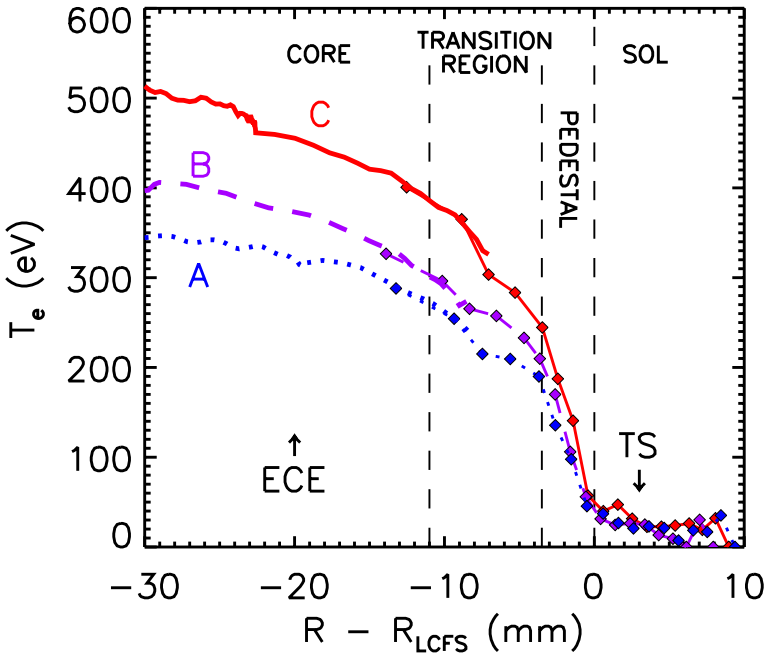

Figure 14: Profiles of T_e obtained from ECE (thick curves) and edge TS (diamonds) in 5.4 T, 0.8 MA discharges with varying levels of input ICRF power $P_{\rm RF}$: 1.6 MW (profile A), 2.1 MW (profile B) and 2.7 MW (profile C). Both pedestal electron temperature $T_{e,\rm PED}$ and maximum T_e gradient $|\nabla T_e|_0$ increase with $P_{\rm RF}$.

To characterize fully the scalings of pedestal parameters with control parameters, multiple regression analysis was performed on the data set described above. For simplicity a power law form was chosen for the fitting function:

$$g = C_0 (I_P)^{\alpha} (\bar{n}_{e,L})^{\beta} (B_T)^{\gamma} (P_{\rm SOL})^{\delta} \tag{5}$$

where g is a given pedestal parameter. Current, field and power during the H-mode are obvious control parameters for studying the pedestal. Somewhat less obvious is the choice of L-mode target density over H-mode line averaged density $\bar{n}_{e,H}$. This is a suitable choice, since the examined discharges utilize no gas puffing or pumping during H-mode and therefore lack density control following an L-H transition. Essentially, the core n_e during H-mode is a "natural" density that is well correlated with the pedestal density: $n_{e,\rm PED} \approx 0.8 \times \bar{n}_{e,H}$. We observe experimentally that higher target densities yield higher values of $\bar{n}_{e,H} \propto n_{e,\rm PED}$. This is reasonable, since the magnitude of the ionization source that fuels the H-mode edge is determined largely by the densities of neutral and atomic hydrogen in the SOL, which in turn have a positive dependence on the rate of fueling needed to obtain the original L-mode density.

To determine the significance of each independent parameter in determining the power law scaling, an additional term F-test is performed,[29] allowing computation of the probability $P_{F,\mu}$ that a given exponent μ ($\mu \in \alpha, \beta, \gamma, \delta$) is representative of a physical correlation, rather than being a result of random scatter. Table 1 contains the results of the regression performed

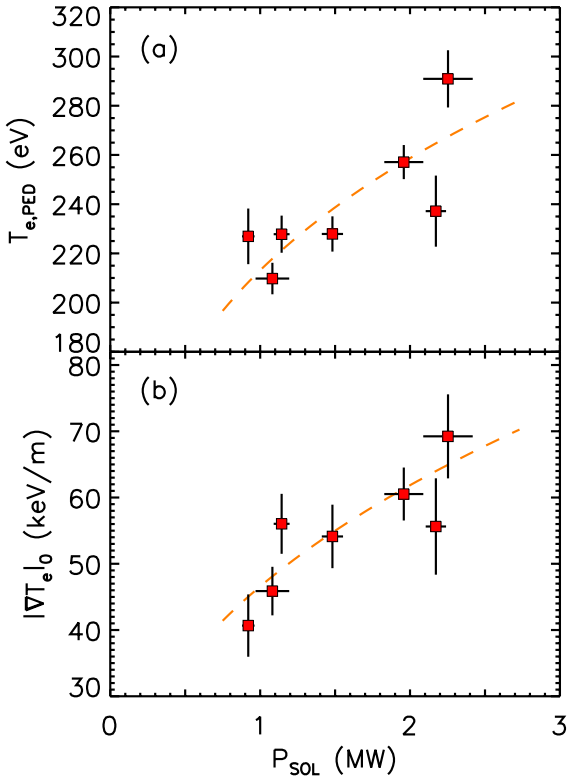

Figure 15: Dependence of (a) pedestal temperature and (b) gradient on power passing into the SOL ($P_{\rm SOL}$). Data are from 5.4 T, 0.8 MA discharges with fixed L-mode target density. Dashed curves represent power law fits to these data. In (a), $T_{e,\rm PED} \sim P_{\rm SOL}^{0.3\pm0.1}$, and in (b), $|\nabla T_e|_0 \sim P_{\rm SOL}^{0.4\pm0.1}$.

on the pedestal widths, tops, and gradients. Listed are the number of points used in each fit, the multiple correlation coefficient R^2, the value of each exponent with its statistical uncertainty, and each $P_{F,\mu}$. For a scaling to be considered significant, we require its $P_{F,\mu}$ be larger than 0.95.

Results of tests for pedestal width scalings are shown in the first three rows of Table 1. The analysis demonstrates that the electron temperature and pressure pedestal widths are largely independent of control parameters. The only correlation of these two widths meeting our criterion for significance is that of Δ_p with $\bar{n}_{e,L}$, and the dependence is unconvincing in light of the very low value of the associated R^2. The n_e width demonstrates a more significant correlation with $(I_P)^{0.8}(B_T)^{-1.0}$, though the R^2 value is relatively low and indicative of considerable scatter in the data set. Despite the scatter, the form of this scaling suggests a correlation between Δ_n and the inverse of edge safety factor. Indeed, regression on 100 points with constant target density using q_{95} as the sole dependent parameter yields $\Delta_n \propto q_{95}^{(-0.90\pm0.15)}$, with $R^2 = 0.27$. This trend is illustrated in Fig. 16.

Scanning I_P, $\bar{n}_{e,L}$, B_T, and $P_{\rm SOL}$ demonstrates varying degrees of effect on the values

Table 1: Results of multiple regression analysis for pedestal parameters as functions of control parameters, assuming scalings of the form $f = (I_P)^{\alpha}(\bar{n}_{e,L})^{\beta}(B_T)^{\gamma}(P_{\rm SOL})^{\delta}$. Included for each exponent μ is the probability $P_{F,\mu}$ that μ is not due merely to random variation, computed using the F-test for additional fitting parameters [Bevington and Robinson, *Data Reduction and Error Analysis for the Physical Sciences*, 2nd ed. (McGraw-Hill, 1992)]

Dep. Param.	No. of points	R^2	I_P exp. α	$P_{F,\alpha}$	$\bar{n}_{e,L}$ exp. β	$P_{F,\beta}$	B_T exp. γ	$P_{F,\gamma}$	$P_{\rm SOL}$ exp. δ	$P_{F,\delta}$
Δ_n	175	0.24	0.79±0.14	>0.99	0.14±0.14	0.67	-0.99±0.29	>0.99	-0.01±0.08	0.10
Δ_T	144	0.03	0.21±0.15	0.84	-0.17±0.15	0.72	-0.05±0.28	0.14	0.15±0.08	0.93
Δ_p	116	0.09	0.14±0.11	0.77	0.28±0.13	0.97	-0.36±0.22	0.89	0.01±0.06	0.06
$n_{e,\rm PED}$	175	0.72	0.94±0.07	>0.99	0.40±0.06	>0.99	-0.46±0.14	>0.99	-0.02±0.04	0.50
$T_{e,\rm PED}$	144	0.63	0.95±0.10	>0.99	-0.78±0.11	>0.99	0.80±0.19	>0.99	0.64±0.06	>0.99
$p_{e,\rm PED}$	116	0.76	1.97±0.12	>0.99	-0.567±0.13	>0.99	0.18±0.22	0.58	0.48±0.06	>0.99
$\lvert\nabla n_e\rvert_0$	175	0.26	0.89±0.13	>0.99	0.01±0.13	0.05	-0.01±0.29	<0.01	-0.07±0.07	0.66
$\lvert\nabla T_e\rvert_0$	144	0.54	1.18±0.13	>0.99	-0.83±0.13	>0.99	0.72±0.23	>0.99	0.53±0.07	>0.99
$\lvert\nabla p_e\rvert_0$	116	0.74	2.03±0.13	>0.99	-0.90±0.14	>0.99	0.44±0.24	0.93	0.46±0.07	>0.99

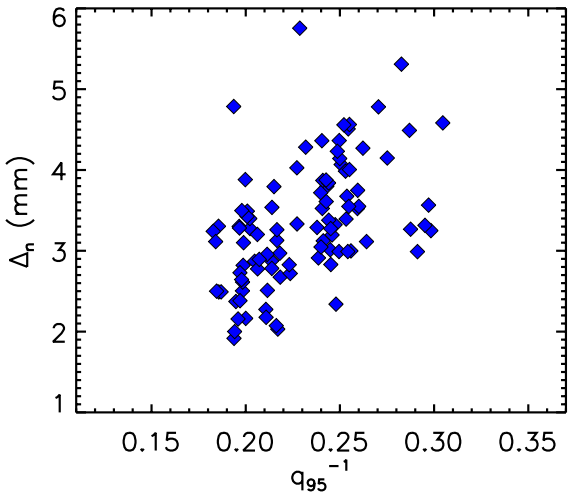

Figure 16: Density pedestal width *vs.* inverse edge safety factor $1/q_{95}$ in EDA H-modes with fixed L-mode target density, $\bar{n}_{e,L} \sim 1.6 \times 10^{20}$ m^{-3}. Higher q favors smaller Δ_n.

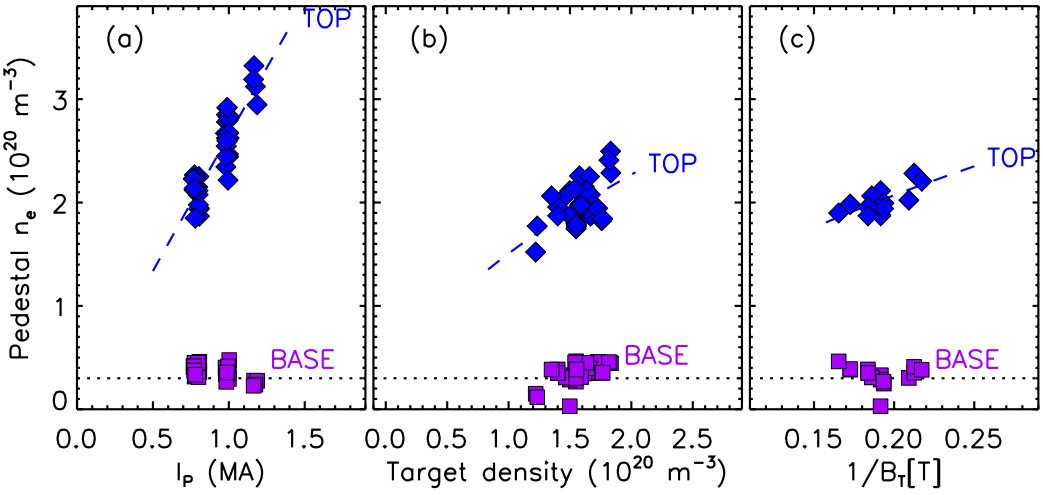

Figure 17: Pedestal n_e, at top (diamonds) and base (squares) of pedestal, *vs.*: (a) plasma current I_P, with fixed toroidal field, $B_T = 5.4$ T and fixed L-mode target density, $\bar{n}_{e,L} \approx 1.5 \times 10^{20}$ m^{-3}; (b) $\bar{n}_{e,L}$, with fixed $B_T = 5.4$ T, $I_P = 0.8$ MA; (c) $1/B_T$, with fixed $I_P = 0.8$ MA, $\bar{n}_{e,L} \approx 1.5 \times 10^{20}$ m^{-3}. Dotted line is the estimated lower limit of the edge TS dynamic range.

atop each pedestal, as shown by rows 4–6 of Table 1. For example, though power is strongly correlated with pedestal T_e, there is virtually no correlation between $P_{\rm SOL}$ and $n_{e,\rm PED}$. The effects on n_e from scanning the other three control parameters is exhibited both in Table 1 and in Fig. 17. In each panel of the figure, two parameters are nominally fixed, while the third density control parameter is varied. Values of n_e at both the top and base of the pedestal are plotted. Because the n_e baseline is typically at the lower limit of the dynamic range of edge TS, it cannot be determined satisfactorily whether the baseline can be correlated with the scanned parameters. The top of the pedestal, however, scales with I_P [17(a)], $\bar{n}_{e,L}$ [17(b)] and $1/B_T$ [17(c)]. Repeating the power law regression of Table 1, row 4 with the insignificant parameter $P_{\rm SOL}$ removed from consideration, we find a predictive scaling:

$$n_{e,\rm PED}[10^{20}\ \rm m^{-3}] = 4.6 \times (I_P[\rm MA])^{0.95\pm0.06} (\bar{n}_{e,L}[10^{20}\ \rm m^{-3}])^{0.39\pm0.06} (B_T[\rm T])^{-0.46\pm0.14} \qquad (6)$$

having $R^2 = 0.72$. The goodness of this fit is illustrated in Fig. 18. Some scatter remains, but to lowest order the predictive scaling reproduces the experimental measurement of $n_{e,\rm PED}$. The scaling is not necessarily complete, of course, since the physics governing the n_e pedestal may be poorly modelled by a simple power law representation using four control parameters. It is also worth noting that the Δ_n scaling mentioned above is qualitatively similar to that of $n_{e,\rm PED}$ on current and field, though the exponents differ somewhat. Whether the width scaling represents actual physics or merely results from the aforementioned $\Delta_n \sim n_{e,\rm PED}$ correlation (Fig. 13) is unclear.

Above it was shown that the T_e pedestal and gradient depend strongly on power through the plasma edge. In fact they exhibit significant variation with each of the control parameters, as shown by the coefficients in rows 5 and 8 of Table 1. Not surprising is that for a given $P_{\rm SOL}$, lower target density results in higher $T_{e,\rm PED}$. Also, there is an linear dependence of $T_{e,\rm PED}$

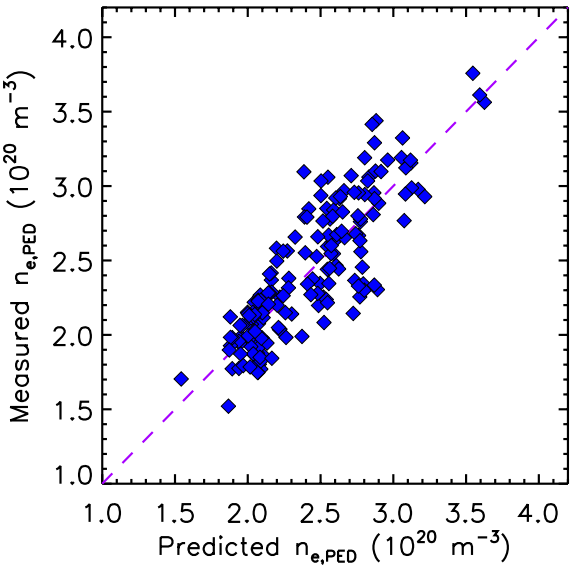

Figure 18: Experimental values of pedestal n_e plotted against values predicted by an empirical scaling obtained by multiple regression on 175 data points: $n_{e,\mathrm{PED}} \propto I_P^{(0.95)} \bar{n}_{e,L}^{(0.39)} B_T^{(-0.46)}$. The fit has a multiple correlation coefficient $R^2 = 0.72$.

on I_P for a given P_{SOL}. This additional I_P dependence implies that the effect of plasma current on the T_e pedestal is not explained solely by the contribution of ohmic power. The T_e pedestal also correlates with B_T, which may be a consequence of changing the ICRF resonance location ($R_{\mathrm{RF}} \propto 1/B_T$) and the resulting alteration to the power deposition profile. Over the range of B_T examined here, the resonance of 80 MHz RF is located at $(R_{\mathrm{RF}} - R)/a$ from -0.5 to 0.3. From Table 1, row 5, the predictive scaling on control parameters for the T_e pedestal is

$$\begin{aligned} T_{e,\mathrm{PED}}[\mathrm{eV}] = 83 \quad &\times \quad (I_P[\mathrm{MA}])^{0.95\pm0.10} (\bar{n}_{e,L}[10^{20}\ \mathrm{m}^{-3}])^{-0.78\pm0.11} \\ &\times \quad (B_T[\mathrm{T}])^{0.80\pm0.19} (P_{\mathrm{SOL}}[\mathrm{MW}])^{0.64\pm0.06} \end{aligned} \tag{7}$$

with $R^2 = 0.63$. When we replace the dependent parameter $\bar{n}_{e,L}$ with $n_{e,\mathrm{PED}}$, the scaling obtained is similar, but with a somewhat poorer $R^2 = 0.54$:

$$\begin{aligned} T_{e,\mathrm{PED}}[\mathrm{eV}] = 154 \quad &\times \quad (I_P[\mathrm{MA}])^{1.13\pm0.18} (n_{e,\mathrm{PED}}[10^{20}\ \mathrm{m}^{-3}])^{-0.50\pm0.13} \\ &\times \quad (B_T[\mathrm{T}])^{0.49\pm0.22} (P_{\mathrm{SOL}}[\mathrm{MW}])^{0.52\pm0.06} \end{aligned} \tag{8}$$

As a consequence of the invariant pedestal width, qualitative statements about the $T_{e,\mathrm{PED}}$ scalings apply equally well to $|\nabla T_e|_0$. The two parameters scale in almost exactly the same manner.

Because $p_{e,\mathrm{PED}} \sim n_{e,\mathrm{PED}} \times T_{e,\mathrm{PED}}$, one would expect the p_e pedestal scalings to have characteristics in common with the n_e and T_e scalings. This is the case, as a clear correlation with current, power and target density is observed, while the toroidal field effects seem largely to cancel. Repeating the regression of Table 1, row 6 without B_T gives

$$p_{e,\mathrm{PED}}[\mathrm{kPa}] = 9.4 \times (I_P[\mathrm{MA}])^{1.98\pm0.11} (\bar{n}_{e,L}[10^{20}\ \mathrm{m}^{-3}])^{-0.56\pm0.13} (P_{\mathrm{SOL}}[MW])^{0.48\pm0.06} \tag{9}$$

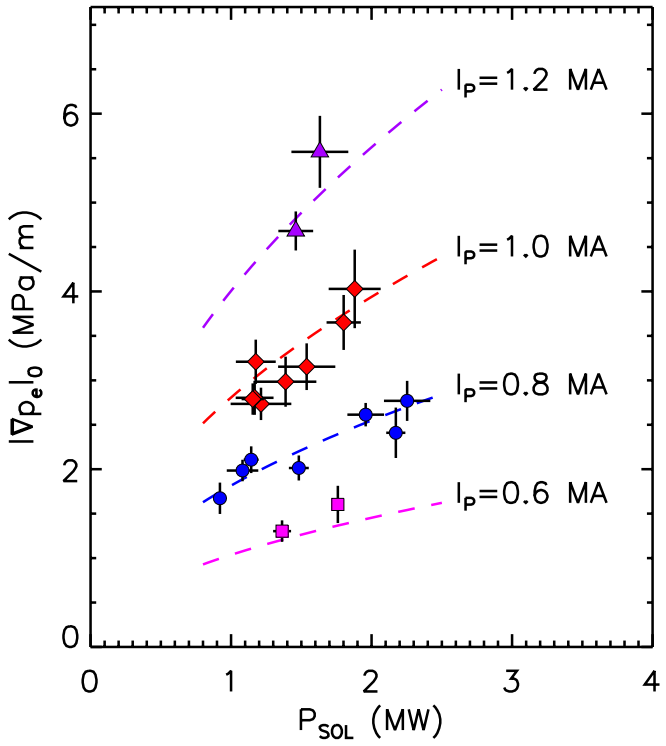

Figure 19: Pedestal electron pressure gradient in EDA pedestals *vs.* $P_{\rm SOL}$ at four distinct values of I_P: 0.6 (squares), 0.8 (circles), 1.0 (diamonds), and 1.2 MA (triangles). The scaling with power is similar to that of the T_e pedestal, while the scaling with current is quite strong. Dashed curves represent the empirical scaling law, $|\nabla p_e|_0 \propto I_P^{(2.0)} P_{\rm SOL}^{(0.5)}$, evaluated at the four noted values of I_P.

with $R^2 = 0.76$. Similar exponents result for the $|\nabla p_e|_0$ scaling. Pressure gradient data from a current scan at constant target density are plotted in Fig. 19 *vs.* $P_{\rm SOL}$, and have been grouped according to I_P. The strong scaling with current demonstrated by the plot is unsurprising, given the linear dependence on current of both $n_{e,\rm PED}$ and $T_{e,\rm PED}$. It is interesting to note that an I_P^2 dependence would be expected in a pedestal limited by ideal ballooning modes, as in type I ELM-ing discharges on ASDEX-Upgrade.[30] However, analysis of C-Mod pedestals demonstrates bootstrap current stabilization of ideal modes and operation above the ballooning limit.[12,31] The scaling $p_{e,\rm PED} \sim P_{\rm SOL}^{1/2}$ is directly related to the similar scaling of the temperature pedestal. Equation 9 reveals too that the strong negative scaling of $T_{e,\rm PED}$ with target density (Eq. 7) is not overcome by the weaker positive scaling of $n_{e,\rm PED}$ with $\bar{n}_{e,L}$ (Eq. 6). Therefore, for a given current and input power, the pressure pedestal actually falls with increasing target density.

Above it was stated that total plasma stored energy scales linearly with $p_{e,\rm PED}$, and in fact we obtain a power law similar to Eq. 9 for W_P:

$$W_P[\rm kJ] = 94 \times (I_P[\rm MA])^{2.08\pm0.07} (\bar{n}_{e,L}[10^{20}\ \rm m^{-3}])^{-0.43\pm0.08} (P_{\rm SOL}[MW])^{0.75\pm0.04} \qquad (10)$$

with $R^2 = 0.92$. Unfortunately it is not entirely straightforward to compare this result to

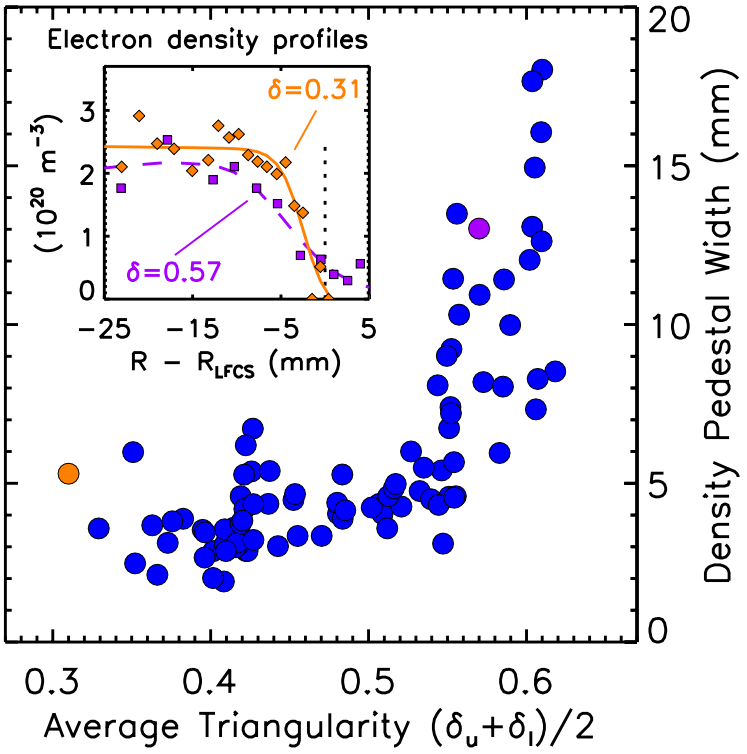

Figure 20: Variation of n_e pedestal width on the average of upper and lower triangularity (δ_u, δ_l) observed during shaping scans. Pedestal heights (inset) change little during a scan. Points shown are in the range: $5.0 < B_T[\mathrm{T}] < 5.6$, $0.7 < I_P[\mathrm{MA}] < 1.3$, $3 < q_{95} < 5$, $1.55 < \kappa < 1.70$.

commonly used cross-machine confinement scalings, due to differing choices of fitting parameters. Power laws determined from analysis of the International Tokamak Experimental Reactor (ITER) confinement database[32] have as a dependent parameter the line averaged H-mode density $\bar{n}_{e,H}$ rather than $\bar{n}_{e,L}$, and use total power loss $P_{\mathrm{LOSS}} = P_{\mathrm{SOL}} + P_{\mathrm{RAD}}$ instead of P_{SOL}. Because of the large covariance of H-mode density and plasma current in C-Mod, and because the radiated power fraction can be considerable (up to 60% in the discharges considered, and strongly dependent on density), attempts to determine scalings of confinement time with the set of parameters I_P, $\bar{n}_{e,H}$ and P_{LOSS} lead to large uncertainties in the power law exponents, and limited agreement is obtained with the ELMy (and ELM-free) H-mode scaling laws of Ref. 32.

Though pedestal widths lack clear correlations with plasma parameters, this could be a consequence of both large scatter in the TS data set and the somewhat restricted range of Δ at the standard C-Mod shape. We see evidence of considerable effects on pedestals due to shaping, which suggests that more strongly shaped plasmas may reveal more Δ variation. When triangularity δ is ramped higher during discharges, a clear increase is observed on the density pedestal width, as illustrated in Fig. 20. Interestingly, no systematic effect was seen on the T_e pedestal width in these scans. The absolute electron temperatures in these particular discharges are not well known due to instrumental reasons, and so the effects

of triangularity on $T_{e,\mathrm{PED}}$ are not determined at this time. Systematic studies of pedestal scalings with shape are planned using the recently expanded range of δ on C-Mod.

V. CONCLUSIONS

We measure T_e and n_e profiles on C-Mod with millimeter resolution TS, and observe H-mode pedestals with typical Δ_n, $\Delta_T \sim$ 2–6 mm. These widths are of the same order as the poloidal ion gyroradius, but do not vary systematically as $\rho_{i,\mathrm{POL}}$ is changed. On average the T_e pedestal is slightly wider than and lies inside the n_e pedestal, with the feet of either pedestal near the LCFS. This average behavior does not preclude pedestals such that $\Delta_n > \Delta_T$; such profiles are in fact commonly measured. Between the T_e pedestal and the core plasma is a transitional region of intermediate T_e gradient approximately 1 cm in radial extent, with temperature a few percent above that of the pedestal. Measurements at both the top and the base of the pedestal are consistent with profiles obtained using other diagnostics.

Characteristic profiles are quite similar in either EDA or ELM-free operation, but some systematic differences have been observed. The presence or absence of the QC mode responsible for EDA can be related to conditions near the edge, in particular edge density, temperature, pressure, and safety factor. Obtaining the QC mode at moderate q_{95} requires a minimum pedestal n_e, while at high q_{95}, a T_e threshold exists for the loss of the mode. The results suggest that both high q and and large collisionality favor the QC mode. There is also evidence that pressure gradient may play a role in the presence or absence of the QC mode at low values of edge q.

Scaling studies of the pedestal at fixed shape yield little systematic variation of widths with plasma parameters, though stronger shaping tends to increase Δ_n dramatically. Measurements of EDA H-modes collected in a pedestal database suggest possible correlations of Δ_n with $n_{e,\mathrm{PED}}$ and with $1/q_{95}$. Pedestal heights and gradients show the clearest dependencies on plasma parameters. The value of $n_{e,\mathrm{PED}}$ scales linearly with I_P, and more weakly with both L-mode target density and inverse B_T. The T_e pedestal top and gradient both scale roughly as $I_P P_{\mathrm{SOL}}^{0.6} (B_T/\bar{n}_{e,L})^{0.8}$, while the p_e pedestal height and gradient both scale with $I_P^2 P_{\mathrm{SOL}}^{1/2}$. The physics underlying these scalings is not completely understood; there is perhaps connection to the physics of the QC mode. Similar scaling laws should be determined for ELM-free H-modes, as well as for discharges exhibiting small ELMs, in order to make a systematic comparison across regimes.

As expected, core confinement depends strongly on edge conditions. In particular we find that W_P scales as $p_{e,\mathrm{PED}}$, implying that confinement scalings may be in large part be determined by scalings of the edge pedestal. Future work will attempt to address the physics underlying the phenomenology and empirical scalings of the pedestal, with the ultimate goal of carefully relating edge transport with global confinement.

ACKNOWLEDGEMENTS

This work was supported by DOE Coop. Agreement No. DE-FC02-99ER54512.

References

[1] M. Greenwald, R.L. Boivin, F. Bombarda, *et al.*, Nucl. Fusion, **37**, 793 (1997).

[2] T.H. Osborne, R.J. Groebner, L.L. Lao, *et al.*, Plasma Phys. Control. Fusion **40**, 845 (1998).

[3] I.H. Hutchinson, R. Boivin, F. Bombarda, *et al.*, Phys. Plasmas **1**, 1511 (1994).

[4] J.W. Hughes, D.A. Mossessian, A.E. Hubbard, E.S. Marmar, D. Johnson, and D. Simon, Rev. Sci. Instrum. **72**, 1107 (2001).

[5] E.S. Marmar, R.L. Boivin, R.S. Granetz, *et al.*, Rev. Sci. Instrum. **72**, 940 (2001).

[6] L.L. Lao, H. St. John, R.D. Stambaugh, A.G. Kellman, and W. Pfeiffer, Nucl. Fusion **25**, 1611 (1985).

[7] B. LaBombard, J.A. Goetz, I. Hutchinson, *et al.*, J. Nucl. Mater. **241–243**, 149 (1997).

[8] R.J. Groebner and T.N. Carlstrom, Plasma Phys. Control. Fusion **40**, 673 (1998).

[9] B. LaBombard, M.V. Umansky, R.L. Boivin, *et al.*, Nucl. Fusion **40**, 2041 (2000).

[10] D.A. Mossessian, A. Hubbard and J. Irby, Rev. Sci. Instrum. **70**, 759 (1999).

[11] D. Mossessian, A.E. Hubbard, E.S. Marmar, *et al.*, Plasma Phys. Control. Fusion **42**, A255 (2000).

[12] A.E. Hubbard , R.L. Boivin, R.S. Granetz, *et al.*, Phys. Plasmas **5**, 1744 (1998).

[13] R.S. Granetz (private communication, 2002).

[14] H. Zohm, Plasma Phys. Control. Fusion **38**, 105 (1996).

[15] Y. Takase, R.L. Boivin, F. Bombarda, *et al.*, Phys. Plasmas **4**, 1647 (1997).

[16] M. Greenwald, R. Boivin, P. Bonoli, *et al.*, Phys. Plasmas **6**, 1943 (1999).

[17] A.E. Hubbard, R.L. Boivin, R.S. Granetz, *et al.*, Phys. Plasmas **8**, 2033 (2001).

[18] J.A. Snipes, B. LaBombard, M. Greenwald, *et al.*, Plasma Phys. Control. Fusion **43**, L23 (2001).

[19] I.H. Hutchinson, R.L. Boivin, F. Bombarda, *et al.*, in *Proceedings of the 16th International Conference on Fusion Energy*, Montreal, 1996 (International Atomic Energy Agency, Vienna, 1997), Vol. 1, p. 155.

[20] Y. Lin, J. Irby, P. Stek, I. Hutchinson, J. Snipes, R. Nazikian, and M. McCarthy, Rev. Sci. Instrum. **70**, 1078 (1999).

[21] A. Mazurenko, Ph.D. thesis, Massachusetts Institute of Technology (2001).

[22] J.W. Connor, R.J. Hastie and J.B. Taylor, Phys. Rev. Lett. **40**, 396 (1978).

[23] A.E. Hubbard, Plasma Phys. Control. Fusion **42**, A15 (2000).

[24] M. Kotschenreuther, W. Dorland, M.A. Beer, and G.W. Hammett, Phys. Plasmas **2**, 2381 (1995).

[25] R.J. Groebner and T.H. Osborne, Phys. Plasmas **5**, 1800 (1998).

[26] T. Hatae, Y. Kamada, S. Ishida, *et al.*, Plasma Phys. Control. Fusion **40**, 1073 (1998).

[27] W. Suttrop, O. Gehre, J.C. Fuchs, H. Reimerdes, W. Schneider, J. Schweinzer, and the ASDEX Upgrade team, Plasma Phys. Control. Fusion **40**, 771 (1998).

[28] R.J. Groebner, Bull. Am. Phys. Soc. **46** (8), 208 (2001).

[29] P.R. Bevington and D.K. Robinson, *Data Reduction and Error Analysis for the Physical Sciences*, 2nd ed. (McGraw-Hill, Boston 1992).

[30] G. Saibene, L.D. Horton, R. Sartori, *et al.*, Nucl. Fusion **39**, 1133 (1999).

[31] D.A. Mossessian, P.B. Snyder, M. Greenwald, J.W. Hughes, Y. Lin, A. Mazurenko, H.R. Wilson, and S. Wolfe in *Proceedings of the 28th Conference on Controlled Fusion and Plasma Physics*, Madeira, 2001 (European Physical Society, 2001), P1.056.

[32] ITER Physics Basis Editors, *et al.*, Nucl. Fusion **39**, 2137 (1999).